FRONTIERS OF PHYSICS

RESEARCH ARTICLE
Volume 21 / Issue 9 / 092202 / 2026

Spatial phase controlled symmetric and asymmetric photoinduced lattice in an atomic ensemble

Muhua Zhai[1,*], Feng Wen[1,†], Zhaotian Sun[1,*], Shaowei Zhang[1], Yang Lei[1], Zhenkun Wu[2], Jiani Li[1], Zhihao Tong[1], Boning Wen[1], Minghui Zhang[1], Yanpeng Zhang[1], Hongxing Wang[1]

1 Key Laboratory for Physical Electronics and Devices of the Ministry of Education & School of Science & Shaanxi Key Laboratory of Information Photonic Technique & Institute of Wide Bandgap Semiconductors & Key Laboratory of Multifunctional Materials and Structures, Ministry of Education, School of Electronic Science and Engineering, Xi'an Jiaotong University, Xi'an 710049, China

2 School of Physics and Electronics, Henan University, Kaifeng 475004, China

*These two authors contributed equally to this work.

Corresponding author. E-mail: †fengwen@mail.xjtu.edu.cn

Received January 11, 2026; accepted April 7, 2026

ABSTRACT

Two-dimensional (2D) photoinduced lattices in atomic ensembles constitute an ideal platform for the systematic investigation of light–matter interactions and controllable diffraction phenomena. Nevertheless, existing research efforts have primarily concentrated on fixed or symmetric lattice configurations, resulting in insufficient exploration of asymmetric diffraction behaviors. Herein, we theoretically propose a 2D phase-controllable photoinduced lattice, which is constructed by overlapping two identical sublattices with independently tunable spatial phases within an atomic ensemble. Spatial phase difference between the two sublattices can be controlled directly by tuning the initial phase of the lattice-forming beams, eliminating the need for complex optical path designs and tedious system optimization. We demonstrate that the absorption, dispersion, and transmission properties of the proposed lattice can be dynamically tuned via photon detuning, leading to the generation of both amplitude- and phase-type lattices. Notably, the amplitude-type lattices exhibit insensitivity to phase variations, whereas the phase-type lattices demonstrate remarkable phase-dependent energy transfer effects and pronounced directional asymmetry. Specifically, a one-dimensional (1D) spatial phase difference between the two identical sublattices induces stripe-like modulation, whereas a 2D spatial phase difference yields reconfigurable anisotropic 2D modulation patterns. Furthermore, we demonstrate that the combined modulation of detuning and spatial phase difference induces periodic asymmetric oscillations in diffraction energy, enabling precisely controllable asymmetric distribution of diffraction. Our work establishes a comprehensive theoretical framework for phase-driven asymmetric diffraction in photoinduced lattices and provides an effective strategy for the development of dynamically reconfigurable all-optical nonreciprocal photonic devices.

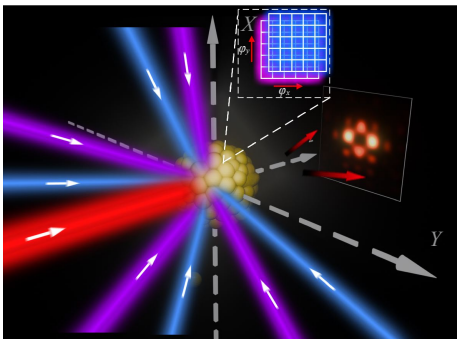

Keywords asymmetric diffraction, spatial phase difference modulation, far-field diffraction, coherent optical effects, phase shift, electromagnetically induced transparency

1 Introduction

Ultracold atoms trapped in optical lattices have emerged as a versatile platform for quantum simulation, enabling the precise realization of complex many-body phenomena in condensed matter physics, including the Bose–Hubbard model [1–3], superfluid-to-Mott insulator transitions [4–7], and topological phases [8–10]. These systems exploit the tunability of laser-induced potentials to manipulate atomic wavefunctions with unprecedented precision, providing a bridge between atomic physics and solid-state analogs [11–14]. In particular, photoinduced lattices, formed via the interference of multiple laser beams in atomic ensembles, allow dynamic reconfiguration of lattice geometries without mechanical limitations, thereby facilitating investigations of light-matter interactions at the quantum level [15–18]. The underlying manipulation mechanism relies on electromagnetically induced transparency (EIT), a quantum interference effect that renders an otherwise opaque atomic medium transparent to a probe field by means of coupling with a strong control field [19–21]. In rubidium atomic systems, EIT has been extensively demonstrated in both hot and cold atomic vapors, giving rise to intriguing phenomena such as slow light, optical storage, and enhanced nonlinear optical effects [22–26]. When integrated with periodic modulation, EIT enables the formation of electromagnetically induced gratings (EIGs). Such gratings feature spatially periodic atomic susceptibility, which diffracts incident light and yields unique diffraction properties [27–29]. EIGs hold promising prospects for applications in all-optical switching, beam splitting, and quantum information processing [30, 31]. In recent years, EIGs have been further extended to two-dimensional (2D) configurations to construct photoinduced lattices, which support more abundant diffraction patterns and symmetry-breaking behaviors [32–39].

To engineer photoinduced lattices in atomic systems and investigate their diffraction properties, researchers have developed a wide range of optical strategies. For instance, the interference of four plane waves in atomic ensembles forms amplitude and phase square lattices, which enable dynamic manipulation of near-field Talbot imaging and far-field Fraunhofer diffraction patterns, thus realizing efficient higher-order diffraction and nondestructive atomic imaging [32]. Furthermore, three-beam laser interference produces tunable honeycomb lattices, allowing effective control over Dirac point positions and their coalescence. This facilitates the study of wavefunction diffraction dynamics in topological phase transitions [38–40]. In Rydberg atomic ensembles, an asymmetric photo-induced lattice can attain tunable high-order diffraction by virtue of van der Waals interatomic interactions and flexible modulation parameters, laying a foundation for accurate diffraction control in such photolattice platforms. Photonic Floquet topological insulators in atomic media enable robust unidirectional light propagation via periodic refractive index modulation, offering an ideal platform for exploring backscattering-free topological edge states and related diffraction phenomena [41–43]. Photonic crystal-derived lattice schemes use extended optical modes to tailor light-matter interactions, thereby improving the characterization of collective diffraction responses and quantum statistical behaviors [44]. Recently, photoinduced moiré lattices created by stacking twisted sublattices have further enhanced diffraction manipulation. By tuning photon detuning, diffraction efficiency and spatial intensity distribution can be flexibly adjusted, deepening the fundamental understanding of light propagation in twisted photonic structures [45–48]. Overall, extensive studies on optical lattices have confirmed the high flexibility of interference-based techniques, laying a solid foundation for the systematic research of photoinduced diffraction properties. However, existing studies have mainly focused on lattices with fixed interference profiles or simple modulation, as well as one-dimensional (1D) and symmetric diffraction patterns. Systematic research on phase-controlled 2D asymmetric diffraction and its coupling with probe detuning is still very limited.

In this paper, we theoretically propose a photoinduced lattice in an atomic ensemble formed by superposing two sublattices, whose optical properties are dynamically reconfigurable by adjusting their spatial phase difference between them. Our results reveal that photon detuning and Rabi frequency regulate lattice transmission and diffraction intensity, achieving a transition between amplitude- and phase-type lattices. Meanwhile, the spatial phase difference between two sublattices dominates diffraction energy distribution and directional reconfiguration of phase-type lattices but is negligible for amplitude-type ones. This photoinduced lattice realizes real-time, non-mechanical reconfiguration with low-power high-efficiency diffraction and precise multidirectional energy manipulation, providing a viable platform for reconfigurable optical field control and a fundamental framework for programmable all-optical photonic devices.

Notably, the proposed scheme has unique advantages and significant scientific and technological value. The multi-beam interference lattice dynamically modulates symmetry and diffraction distribution by tuning the spatial phase difference between two sublattices and frequency detuning without altering the optical system geometry. Precise probe detuning controls the real and imaginary optical response components to realize continuous transition between amplitude- and phase-type lattices, thereby achieving controllable energy redistribution between zeroth- and higher-order diffractions (providing a new method for precise spatial light field manipulation). In addition, the moiré twisted lattices can be constructed via sublattice interlayer coupling and

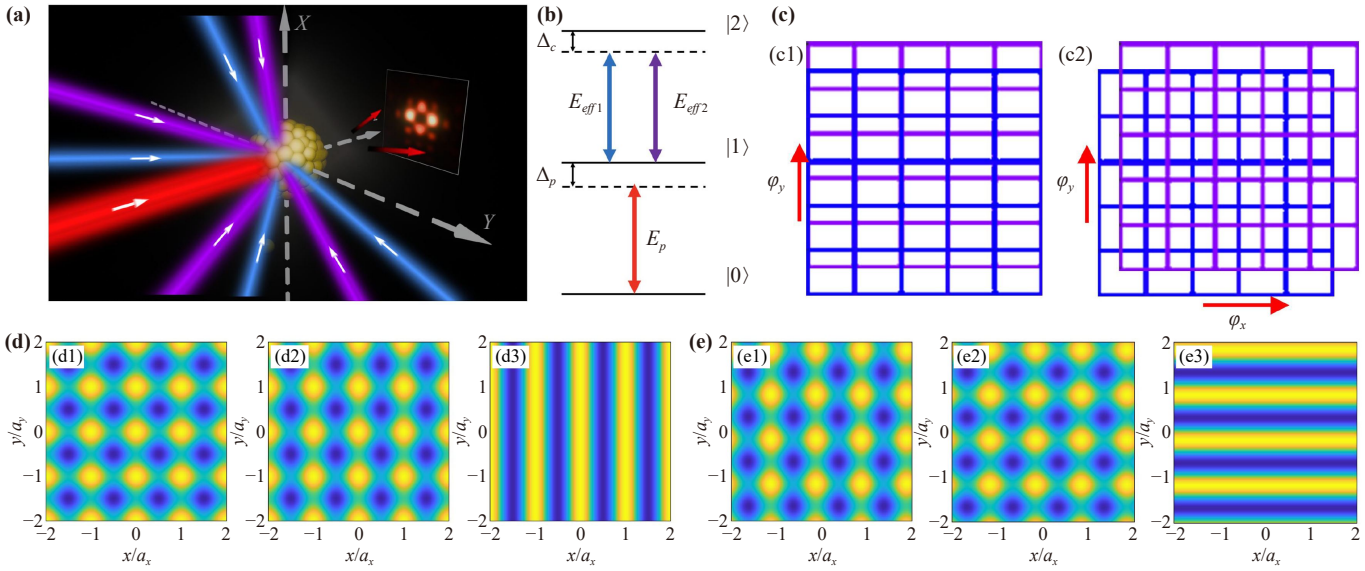

Fig. 1 **(a)** The geometry of photoinduced lattice and the corresponding far-field diffraction patterns. **(b)** Cascade-type three-level scheme of the ^{85}Rb with $|0\rangle$, $|1\rangle$, and $|2\rangle$. **(c)** Schematic diagrams of photoinduced lattices with (c1) 1D and (c2) 2D spatial phase difference. **(d)** Spatial phase difference between two sublattices (d1) $\varphi_x = 0$ and $\varphi_y = 0$, (d2) $\varphi_x = 0$ and $\varphi_y = \pi/4$, and (d3) $\varphi_x = 0$ and $\varphi_y = \pi/2$. **(e)** Spatial phase difference control between the two sublattices (e1) $\varphi_x = \pi/4$ and $\varphi_y = \pi/3$, (e2) $\varphi_x = \pi/3$ and $\varphi_y = \pi/3$, and (e3) $\varphi_x = \pi/2$ and $\varphi_y = \pi/3$.

relative rotation angle tuning to extend the system's applicability.

2 Theoretical model

The construction of the photoinduced lattice is predicated on the periodic modulation of the refractive index within an atomic (or molecular) ensemble. As illustrated in Fig. 1(a), our model consists of eight strong control fields E_c, a weak probe field E_p, and an ensemble of closed three-level cascade-type ultra-cold atoms (or molecules) comprising a ground state $|0\rangle$ $(5S_{1/2}(F=3))$, a metastable state $|1\rangle$ $(5P_{3/2}(F=3))$ and an excited state $|2\rangle$ $(5D_{5/2})$, as shown in Fig. 1(b). A weak probe field E_p (with frequency ω_p, wave vector k_p, and Rabi frequency Ω_p) propagates along the z-axis and couples the $|0\rangle \to |1\rangle$ transition, with frequency detuning defined as $\Delta_p = \omega_p - \omega_{10}$. Eight strong control fields E_c (with frequency ω_c, wave vector k_c, and Rabi frequency Ω_c) undergo mutual interference to form an effective lattice field E_{eff} (Rabi frequency Ω_{eff}), thereby establishing a photoinduced lattice structure within the atomic medium. The lattice-forming field $E_{eff}(x,y)$, originating from the same laser, is coherently coupled with the levels $|1\rangle$ and $|2\rangle$, being detuned with $\Delta_c = \omega_c - \omega_{21}$. This results in an EIT if $\Delta_p + \Delta_c = 0$ and $\Omega_p \ll \Omega_{eff}(x,y)$.

Specifically, four coupling beams (denoted as blue beams) function as one set of sublattice-forming laser fields. Among these, two laser beams, symmetrically offset relative to the z-axis, are incident on the atomic sample at a small angle α_x, while the other two laser beams, incident symmetrically around the z-axis at small angles α_y, intersect to generate standing waves along the x- and y-axes within the atomic ensemble, respectively. A 2D optically induced sublattice can be formed within the ultra-cold atomic (or molecular) ensemble when the condition $\Omega_c \gg \Omega_p$ is fulfilled. The effective Rabi frequency of the lattice can be mathematically expressed as $|\Omega_{eff1}(x,y)|^2 = |\Omega_c \sin(\pi x/d_x)|^2 + |\Omega_c \sin(\pi y/d_y)|^2$. Herein, $\Omega_c = \mu_{21}E_c/\hbar$ denotes the Rabi frequency of the coupling field, μ_{ij} represents the transition dipole moment between energy levels $|i\rangle$ and $|j\rangle$, and $d_{x(y)} = \lambda_c/(2\sin\alpha_{x(y)})$ is the spatial period of the sublattice along the $x(y)$-axis. By adjusting the value of $\alpha_x(\alpha_y)$, $d_{x(y)}$ can be arbitrarily tuned to be larger than the wavelength λ_c of the coupling fields. The remaining four coupling beams (denoted as purple beams) constitute a second set of sublattice-forming laser fields, which carry spatial phase difference φ_x and φ_y along the x- and y-axes relative to the first set. This configuration yields an additional sublattice with the same spatial period $d_{x(y)} = \lambda_c/(2\sin\alpha_{x(y)})$, and its corresponding effective Rabi frequency is given by $|\Omega_{eff2}(x,y)|^2 = |\Omega_c \sin(\pi x/d_x + \varphi_x)|^2 + |\Omega_c \sin(\pi y/d_y + \varphi_y)|^2$. Consequently, the total effective Rabi frequency of the entire lattice system can be formulated as $|\Omega_{eff}(x,y)|^2 = |\Omega_{eff1}(x,y)|^2 + |\Omega_{eff2}(x,y)|^2$.

A photoinduced lattice is constructed by superimposing two sublattices with distinct spatial phases. As illustrated in Fig. 1(c1), when spatial interference is introduced

exclusively along a single dimension, the resultant structure forms an EIG. Conversely, when spatial interference is applied along both orthogonal dimensions, the system forms a 2D photoinduced spatial lattice, as shown in Fig. 1(c2). By precisely tuning the spatial phase difference, the symmetry features and spatial distribution of lattice patterns can be flexibly modulated, whereas the global periodicity of the lattice remains invariant. For the EIG, varying the phase difference between the two sublattices greatly modulates their superposition interference pattern. At a specific phase value ($\varphi_x = 0$ and $\varphi_y = 0$), the pattern exhibits high 2D symmetry, as shown in Fig. 1(d1). As the phase difference rises to a certain value $\varphi_y = \pi/4$, the global 2D periodicity remains intact, whereas the intensity distribution of the two sublattices shifts evidently, thereby tailoring the symmetry properties of the lattice pattern. Namely, the symmetry along the y-direction is partially broken, as shown in Fig. 1(d2). When the phase difference further increases to $\varphi_y = \pi/2$, the field modulation along the y-direction changes drastically, rendering the y-direction symmetry fully broken while preserving the intrinsic symmetry along the x-direction, as shown in Fig. 1(d3). Similarly, with the continuous variation of the phase difference φ_x, the x-direction symmetry is broken, whereas the intrinsic y-direction symmetry is well preserved, as illustrated in Figs. 1(e1)–(e3). In other words, the global symmetry of the lattice remains intact, whereas the superposition interference pattern undergoes tunable variations upon the modulation of the spatial phase difference. The transition of the lattice spatial distribution from a 2D to a 1D configuration originates from the relative phase between the two sublattices induced by the spatial phase difference. This relative phase gives rise to destructive interference, particularly at a spatial phase difference of $\pi/2$, where it induces complete destructive interference along one direction, thereby yielding a 1D fringe pattern with an underlying background potential.

From the analysis based on dressed-state theory [49], the atomic transition $|1\rangle \rightarrow |2\rangle$ is periodically dressed by the control field $E_{eff}(x, y)$, and the energy level $|1\rangle$ is then split into two dressed states $|+\rangle$ and $|-\rangle$ with corresponding eigenvalues $\lambda_{\pm} = \Delta_c/2 \pm \sqrt{\Delta_c^2/4 + |\Omega_{eff}(x, y)|^2}$. The optical response of the atomic medium to the probe field is governed by the equation of motion for the density matrix, which in the interaction picture reads $\partial\rho/\partial t = -\mathrm{i}/\hbar\,[\rho, H_{\mathrm{int}}]$. Based on the energy-level scheme shown in Fig. 1(b), and under the rotating-wave approximation [50], the interaction Hamiltonian between the atomic ensemble and laser fields can be expressed as

$$H_{\mathrm{int}} = \Omega_p \mathrm{e}^{-\mathrm{i}\Delta_p t} |0\rangle\langle 1| + \Omega_{eff} \mathrm{e}^{-\mathrm{i}\Delta_c t} |1\rangle\langle 2| + h.c., \quad (1)$$

where $\Omega_p = \mu_{10} E_p/\hbar$. $h.c.$ denotes the Hermitian conjugate. By solving the density-matrix equation under the weak probe-field approximation, the induced polarization at the probe frequency can be written as

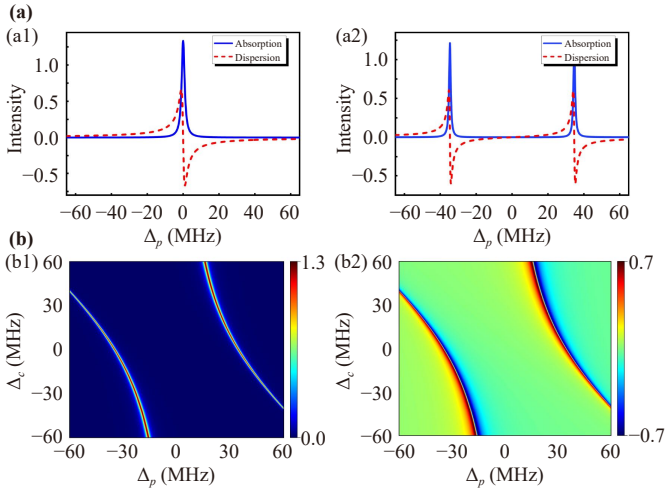

Fig. 2 **(a)** Absorption spectrum and dispersion spectrum at the nodes (a1) and antinodes (a2) of the lattice-forming laser. **(b)** Absorption spectrum (b1) and dispersion spectrum (b2) of the atomic ensemble as functions of Δ_c and Δ_p.

$P(\omega_p) = \omega_0 \chi(\omega_p) E_p$, where the optically induced susceptibility is given by

$$\chi(\omega_p) = \frac{\mathrm{i}N|\mu_{10}|^2}{\hbar\varepsilon_0} \frac{d_{20}}{d_{10}d_{20} + |\Omega_{eff}|^2}. \quad (2)$$

Here, N is the atomic density, ε_0 is the vacuum permittivity, $d_{10} = \gamma_{10} - \mathrm{i}\Delta_p$, $d_{20} = \gamma_{20} - \mathrm{i}(\Delta_p + \Delta_c)$, and γ_{ij} is the dephasing rate between levels $|i\rangle$ and $|j\rangle$.

Equation (2) indicates that the optical susceptibility $\chi(\omega_p)$ is periodically modulated by the spatial distribution of the lattice-forming field, with its magnitude within a single lattice period significantly regulated by parameters such as Ω_c, Δ_p, Δ_c. To clarify the modulation mechanism, Figs. 2(a1) and (a2) compare the optical properties of the probe field at the nodes and antinodes of the photoinduced lattice. The absorption profiles (solid lines) show the probe field undergoes substantial absorption at lattice nodes, while nearly complete transmission is achieved at antinodes, inducing prominent amplitude modulation. The dispersion curves (dashed lines) reveal positive dispersion at nodes and negative dispersion at antinodes, confirming the feasibility of strong phase modulation. As depicted in Fig. 2(b1), Δ_p and Δ_c effectively modulate the EIT window's position and width by splitting the metastable energy level $|1\rangle$ into two sublevels $|+\rangle$ and $|-\rangle$, enabling spatial periodic modulation of the probe field's amplitude and phase within the x–y plane. Under the slowly varying envelope approximation (SVEA), the propagation behavior of the probe field in the atomic medium is governed by Maxwell's wave equation [51]:

$$\frac{\partial E_p}{\partial z} = \left(-\frac{\alpha}{2} + \mathrm{i}\sigma\right) E_p, \quad (3)$$

where $\alpha = (4\pi/\lambda_p)\,\mathrm{Im}[\chi(\omega_p)]$, and $\sigma = (2\pi/\lambda_p)\mathrm{Re}[\chi(\omega_p)]$ are the absorption and phase-shift coefficients, respectively, and λ_p is the wavelength of the probe field. By solving Eq. (3), the transmission function $T(x,y)$ of the probe beam over an interaction length L can be obtained as

$$T(x,y) = \exp\left[-\frac{\alpha(x,y)L}{2} + \mathrm{i}\sigma(x,y)L\right]. \tag{4}$$

We analyze the far-field diffraction pattern based on Fraunhofer diffraction theory [52]. The pattern is determined by the Fourier transform of $T(x,y)$. Here, the incident probe beam is treated as a plane wave, and the diffraction intensity distribution is given by

$$I(\theta_x,\theta_y) = |E(\theta_x,\theta_y)|^2 \times \frac{\sin^2[M\pi d_x \sin(\theta_x)/\lambda_p]}{M^2\sin^2[\pi d_x \sin(\theta_x)/\lambda_p]} \times \frac{\sin^2[N\pi d_y \sin(\theta_y)/\lambda_p]}{N^2\sin^2[\pi d_y \sin(\theta_y)/\lambda_p]}, \tag{5}$$

where $E(\theta_x,\theta_y) = \iint \mathrm{d}x\mathrm{d}y T(x,y)\exp(-\mathrm{i}2\pi x d_x \sin(\theta_x)/\lambda_p)\cdot\exp(-\mathrm{i}2\pi y d_y \sin(\theta_y)/\lambda_p)$ represents the Fraunhofer diffraction field from a single spatial period. The diffraction efficiency for an arbitrary diffraction order along the x- and y-axes is defined via the grating equations $d_x \sin\theta_x = m\lambda_p$ and $d_y \sin\theta_y = n\lambda_p$. Here, M and N denote the number of illuminated spatial periods along the x- and y-directions, respectively. d_x and d_y are the lattice periods along the x- and y-axes. θ_x and θ_y are the corresponding diffraction angles in the x- and y-directions, respectively.

3 Results and discussion

As elaborated in Section 2, a theoretical investigation is performed to explore the construction of photoinduced lattice through the interference of two sublattice-forming fields propagating within an atomic ensemble. Specifically, a cloud of trapped atoms, confined within a standard cold magneto-optical trap (MOT), is taken into account, with a nominal diameter of approximately 1 mm, while the temperature of the vapor cell is stabilized at ~4.4 mK. The coupling beam, characterized by a wavelength of $\lambda_c = 775.98$ nm, is generated from a continuous-wave (CW) Ti:Sapphire laser and utilized to drive the upper atomic transition $|1\rangle \to |2\rangle$ $[5P_{3/2}(F=3) \to 5D_{5/2}]$. Meanwhile, a weak probe beam (with wavelength $\lambda_p = 780$ nm and power $P_p = 5$ mW) is generated by an external cavity diode laser to couple the lower atomic transition $|0\rangle \to |1\rangle$ $[5S_{1/2}(F=3) \to 5P_{3/2}(F=3)]$. The coupling beam is expanded by means of a beam expander to enhance the effective area of the resulting standing wave, and subsequently split into two identical beams using a beam splitter (BS).

A 2D phase-controllable photoinduced lattice is generated by superposing two sublattices. The first sublattice-forming lasers are symmetrically placed at small angles to the z-axis, and intersect at the center of the atomic vapor cell, inducing a 2D periodically modulated optical field in the x–y plane. The second set follows the same process but with phase plates inserted in the standing waves to introduce an additional phase difference relative to the first sublattice. In addition, a stable optical platform, precise optical path alignment, and temperature control modules are adopted to ensure the long-term stability and strict symmetry of the two sublattices [53, 54]. By configuring the coupling and probe beams in a small-angle paraxial manner and utilizing a two-photon Doppler-free setup, the far-field diffraction pattern of the photoinduced lattice can be clearly observed.

We first analyze the amplitude-type photoinduced lattice when a unidirectional relative phase difference is introduced between two sublattices, by setting $\varphi_x = 0$ and $\Delta_p = \Delta_c = 0$ MHz. Figures 3(a) and (b) illustrate the transmission and phase modulation of the amplitude-type photoinduced lattice across four spatial periods. As depicted in Fig. 3(a1), when $\varphi_y = 0$, the transmission function $T(x,y)$ presents a series of discrete sharp peaks with symmetric and periodic properties along the x- and y-directions. This phenomenon arises from nearly full light transmission at the antinodes and strong absorption at the nodes, which induces periodic amplitude modulation of the probe beam. As the relative phase difference φ_y increases, the transmission intensity gradually decays along the y-direction while remaining nearly invariant along the x-direction, as illustrated in Figs. 3(a2) and (a3). Ultimately, as φ_y rises to $\pi/2$, $T(x,y)$ exhibits a striped profile along the x-direction and turns nearly uniform along the y-direction, which corresponds to a 1D periodic lattice, as shown in Fig. 3(a4). It should be emphasized that the real part of the atomic susceptibility vanishes under $\Delta_p = 0$ MHz, so no phase modulation is induced. Accordingly, the phase of $T(x,y)$ remains consistently zero, as shown in Figs. 3(b1)–(b4). Consequently, the lattice behaves similarly to a pure amplitude-type photoinduced lattice. The corresponding Fraunhofer diffraction patterns of photoinduced lattice are presented in Figs. 3(c). Since pure amplitude modulation only redistributes light intensity via absorption, the diffracted intensity is always confined to the zeroth-order and remains independent of the relative phase difference φ_y, as shown in Figs. 3(c1)–(c4). This is a typical feature of an ideal amplitude grating.

Subsequently, a phase-type photoinduced lattice is constructed by setting $\Delta_p = 21.21$ MHz and $\Delta_c = 0$ MHz. In this scheme, the coupling fields are maintained at a relatively high intensity to resonantly interact with the atomic transition $|1\rangle \to |2\rangle$, thereby ensuring high transparency of the probe field. The weak probe field is properly detuned from the transition $|0\rangle \to |1\rangle$, i.e., $|\Omega_{eff}(x,y)| \approx |\Delta_p|$, while remaining within the EIT window, which enables the achievement of π phase

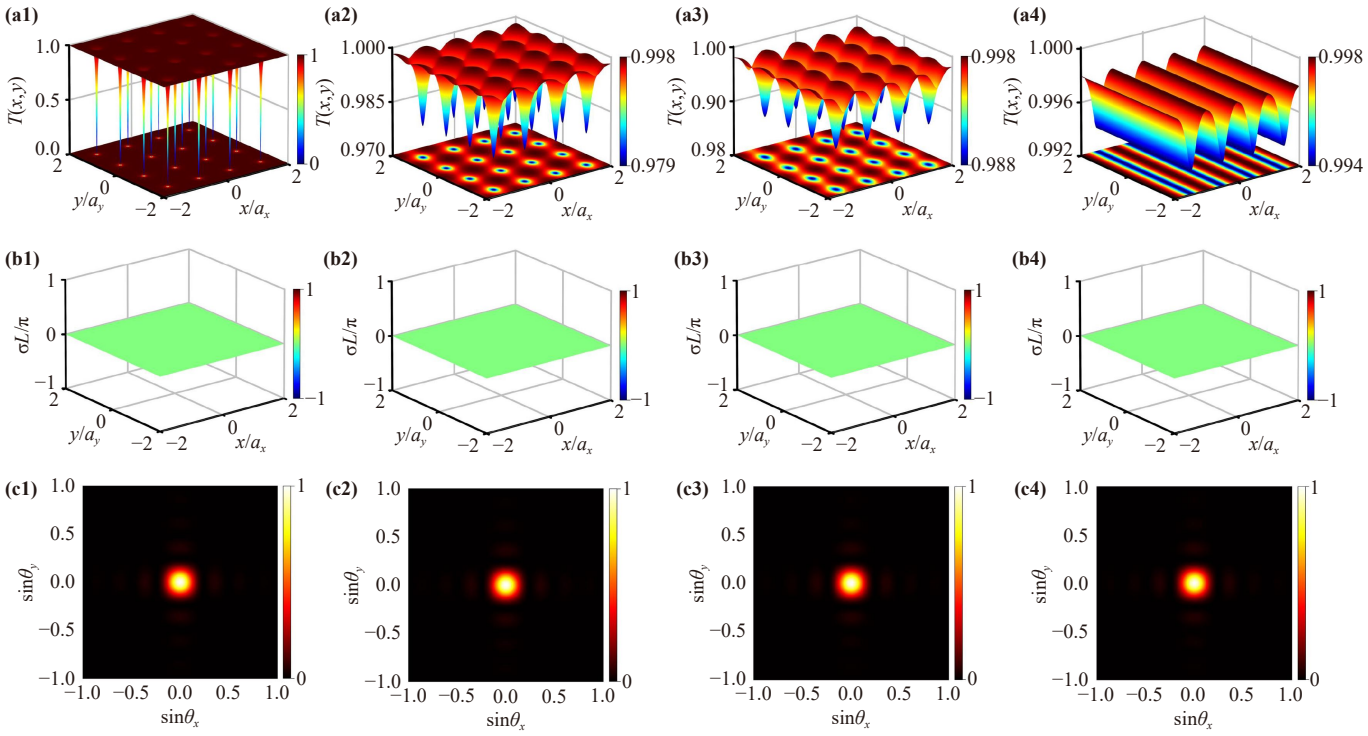

Fig. 3 Amplitude-type photoinduced lattice. **(a1–a4)** The intensity and **(b1–b4)** the phase of $T(x,y)$ with different spatial phase difference between the two sublattices, (a1) and (b1) $\varphi_y = 0$, (a2) and (b2) $\varphi_y = \pi/4$, (a3) and (b3) $\varphi_y = \pi/3$, and (a4) and (b4) $\varphi_y = \pi/2$. **(c1–c4)** The corresponding diffraction patterns. Other parameters are $\varphi_x = 0$, $\Omega_c = 15$ MHz, $\Delta_p = 0$ MHz, $\Delta_c = 0$ MHz, $\gamma_{10} = 1$ MHz, $\gamma_{20} = 0.1$ MHz, $L = 12$, and $M = N = 1$.

modulation. Accordingly, both absorption and phase change abruptly, with the zeroth-order diffraction energy redistributed into higher-order components. As the two sublattices are fully in phase ($\varphi_x = 0$ and $\varphi_y = 0$), the intensity distribution of $T(x,y)$ demonstrates that the probe field exhibits high transmittance at both the nodes and antinodes of the lattice. Its overall contrast is much higher than that of amplitude-type photoinduced lattices, as illustrated in Fig. 4(a1). Moreover, the transmission phase of $T(x,y)$ is no longer zero, as presented in Fig. 4(b1). This is a typical feature of an ideal phase-type photoinduced lattice. From the corresponding far-field diffraction pattern, as depicted in Fig. 4(c1), it can be seen that compared with Fig. 3(c1), the energy of zeroth-order diffraction is greatly reduced. In contrast, the first-order diffraction intensities along the x- and y-directions, as well as in the four quadrants, are remarkably enhanced. This behavior originates from the periodic variation of the real part of the susceptibility $\mathrm{Re}(\chi)$. As the spatial phase difference between the two sublattices along the y-direction φ_y increases from 0 to $\pi/2$, both the intensity and phase distributions of $T(x,y)$ gradually become uniform along the y-direction and eventually evolve into a 1D periodic stripe structure, as presented in Figs. 4(a1)–(a4) and (b1)–(b4), respectively. Meanwhile, the corresponding far-field diffraction pattern reveals that the diffraction intensity along the y-direction gradually decays, and the energy is progressively concentrated within $I(\theta_x^1, \theta_y^0)$, as illustrated in Figs. 4(c2) and (c3). At $\varphi_y = \pi/2$, the first-order and higher-order diffractions along the y-direction almost completely vanish. Most of the energy is confined to the central diffraction orders $I(\theta_x^1, \theta_y^0)$, with only a small fraction distributed in the first-order diffractions located in four quadrants, as shown in Fig. 4(c4). This represents a typical characteristic of an ideal phase-type grating.

To quantitatively investigate how the 1D spatial phase difference between the two sublattices modulates the far-field intensity distribution and diffraction symmetry of photoinduced amplitude- and phase-type lattices, we analyze the diffraction intensity profiles along three typical directions under fixed $\varphi_x = 0$, as illustrated in Figs. 5(a1) and (b1), respectively. The dotted lines mark three representative diffraction directions, the horizontal direction is defined by setting $\sin\theta_y = 0$, the vertical direction by setting $\sin\theta_x = 0$, and the diagonal direction by setting $\sin\theta_x = \sin\theta_y$. As shown in Figs. 5(a2)–(a4), for the amplitude-type lattice, the optical energy is predominantly confined to the zeroth-order diffraction, forming a highly symmetric profile. The variation of φ_y has a negligible effect on the diffraction intensity distribution. In contrast, for the phase-type lattice shown in Figs. 5(b2)–(b4), the diffraction intensity deviates from the central region and varies periodically

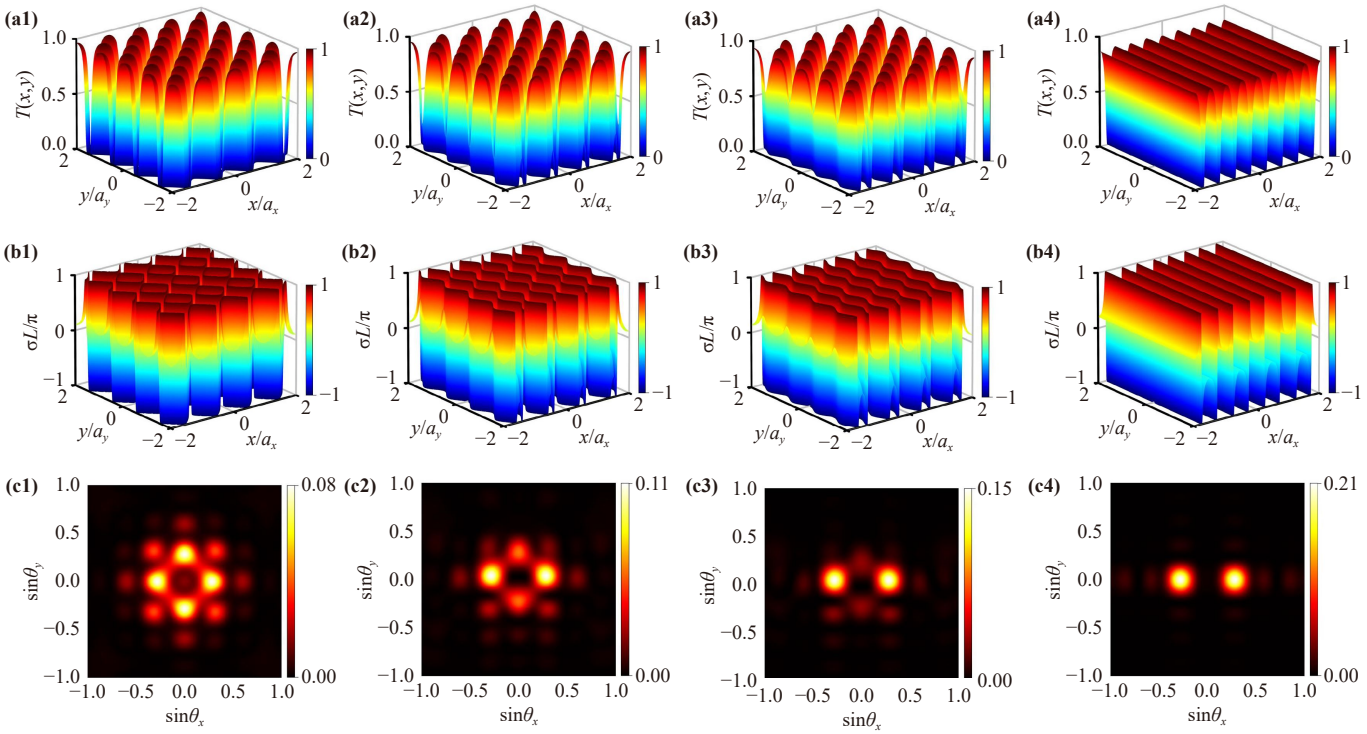

Fig. 4 Phase-type photoinduced lattice. **(a1–a4)** The intensity and **(b1–b4)** the phase of $T(x,y)$ with different spatial phase difference between the two sublattices, (a1) and (b1) $\varphi_y = 0$, (a2) and (b2) $\varphi_y = \pi/4$, (a3) and (b3) $\varphi_y = \pi/3$, and (a4) and (b4) $\varphi_y = \pi/2$. **(c1–c4)** The corresponding diffraction patterns. Other parameters are $\varphi_x = 0$, $\Omega_c = 15$ MHz, $\Delta_p = 21.21$ MHz, $\Delta_c = 0$ MHz, $\gamma_{10} = 1$ MHz, $\gamma_{20} = 0.1$ MHz, $L = 12$, and $M = N = 1$.

with φ_y. Along the vertical direction, the diffraction intensity distribution in Fig. 5(b2) is symmetric with respect to the central axis $\sin\theta_x = 0$, while those in Figs. 5(b3) and (b4) exhibit centrosymmetry.

We also examine diffraction intensity profiles of photoinduced amplitude- and phase-type lattices along

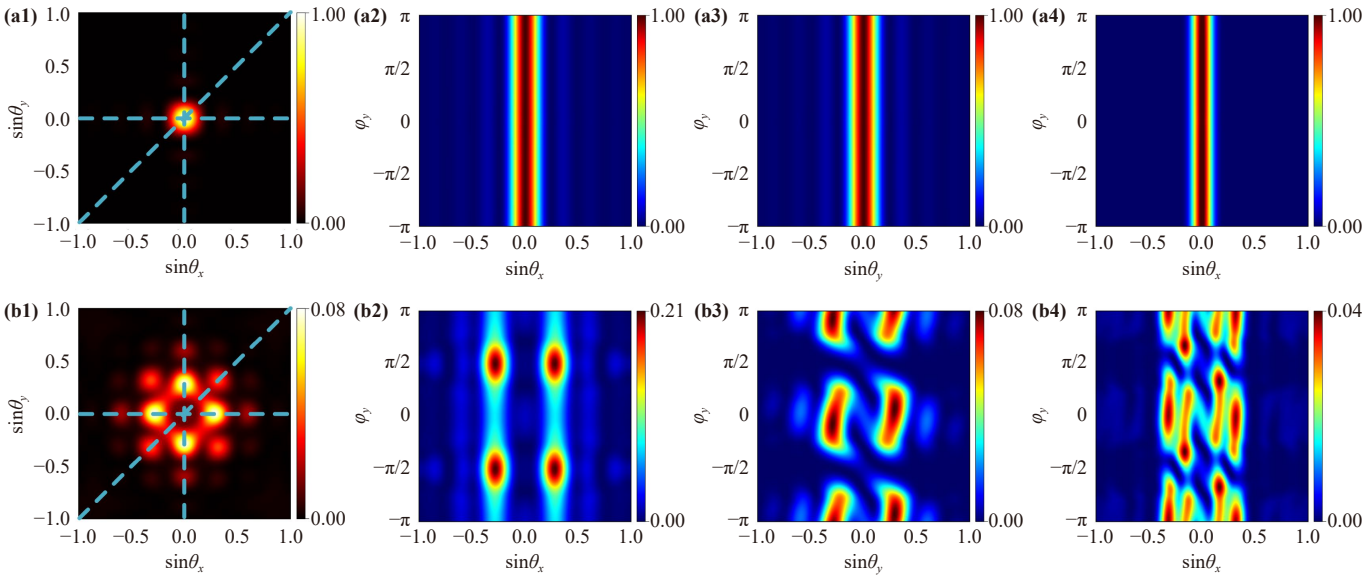

Fig. 5 **(a1, b1)** show the far-field diffraction patterns of the amplitude- and phase-type lattices, respectively. **(a2–a4)** and **(b2–b4)** show the effects of the 1D spatial phase difference on the diffraction intensity distributions along (a2) and (b2) $\sin\theta_y = 0$, (a3, b3) $\sin\theta_x = 0$, and (a4, b4) $\sin\theta_x = \sin\theta_y$. Other parameters $\varphi_x = 0$, $\Omega_c = 15$ MHz, $\gamma_{10} = 1$ MHz, $\gamma_{20} = 0.1$ MHz, $L = 12$, and $M = N = 1$.

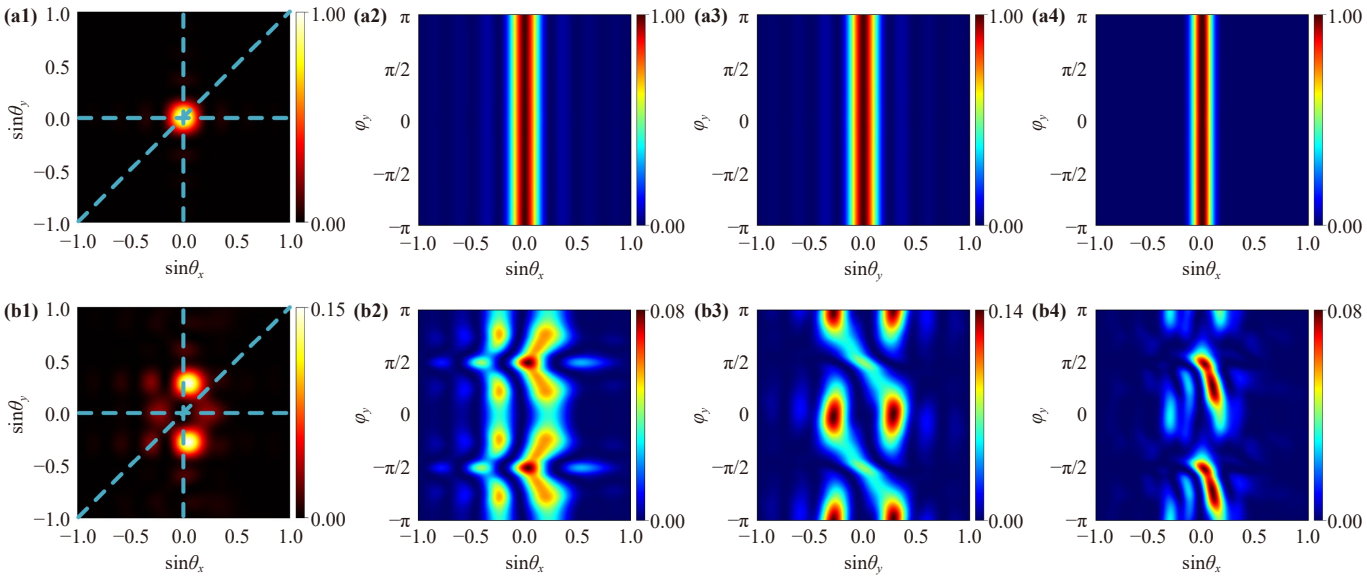

Fig. 6 **(a1, b1)** show the far-field diffraction patterns of the amplitude- and phase-type lattices, respectively. **(a2–a4)** and **(b2–b4)** show the effects of the 2D spatial phase difference on the diffraction intensity distributions along (a2) and (b2) $\sin\theta_y = 0$, (a3, b3) $\sin\theta_x = 0$, and (a4, b4) $\sin\theta_x = \sin\theta_y$. Other parameters $\varphi_x = \pi/3$, $\Omega_c = 15$ MHz, $\gamma_{10} = 1$ MHz, $\gamma_{20} = 0.1$ MHz, $L = 12$, and $M = N = 1$.

three typical directions with fixed $\varphi_x = \pi/3$, as shown in Figs. 6(a1) and (b1). For the amplitude-type lattice, as shown in Figs. 6(a2)–(a4), the diffraction energy is confined to the zeroth-order and insensitive to the spatial phase difference φ_y. In contrast, for the phase-type lattice, as shown in Figs. 6(b2)–(b4), the diffraction energy redistributes periodically with the spatial phase difference φ_y, accompanied by a notable decline in overall symmetry. As depicted in Fig. 6(b2), the symmetry of the diffraction intensity distribution is broken, and the energy of the first-order diffraction $I(\theta_x^1, \theta_y^0)$ is gradually coupled into the zeroth-order $I(\theta_x^0, \theta_y^0)$, which becomes dominant at $\pi/2$. As φ_y further varies from $\pi/2$ to π, the energy shifts back to $I(\theta_x^1, \theta_y^0)$. Figure 6(b3) further reveals that the diffraction pattern maintains asymmetry with respect to the $\sin\theta_y = 0$-axis, and $I(\theta_x^0, \theta_y^1)$ peaks at $\varphi_y = 0$ and $\pm\pi$, while $I(\theta_x^0, \theta_y^0)$ dominates at $\varphi_x = \pm\pi/2$. A comparison of Figs. 6(b2) and (b3) indicates that $I(\theta_x^1, \theta_y^0)$ is markedly lower than $I(\theta_x^0, \theta_y^1)$. In both cases, the diffraction energy gradually couples into the zeroth-order as φ_y increases from 0 to $\pi/2$. As shown in Fig. 6(b4), $I(\theta_x^1, \theta_y^1)$ carries negligible energy, with only faint peaks emerging at $\pm\pi/2$.

Next, we explore the photoinduced lattice with a 2D spatial phase difference. Unlike its 1D counterpart, this structure supports additional spatial phase difference components along both the x- and y-directions. With $\varphi_y = \pi/3$ fixed, we examine the far-field diffraction features of amplitude- and phase-type lattices under different 2D spatial phase difference, as depicted in Figs. 7(a1)–(a4) and (b1)–(b4). For the amplitude-type lattice, diffraction energy is confined mainly to the zeroth-order, as illustrated in Figs. 7(a1)–(a4) and barely varies with spatial phase difference. The diffraction patterns retain high symmetry, revealing strong robustness of energy distribution against phase modulation. In contrast, the phase-type lattice exhibits flexible and tunable diffraction behavior. The symmetry of its diffraction pattern is highly sensitive to phase settings, as illustrated in Figs. 7(b1)–(b4). Under fixed $\varphi_x = 0$ the diffraction intensity is mainly localized at the first-order peaks and maintains horizontal symmetry, as shown in Fig. 7(b1). With an increase in the phase φ_x, diffraction energy is redistributed from higher diffraction orders to lower ones. Meanwhile, the principal diffraction lobe shifts along the x- to y-direction, as illustrated in Fig. 7(b2), which fully disrupts the original biaxial symmetry. When two key parameters are set to $\varphi_x = \pi/3$ and $\varphi_y = \pi/3$, the diffraction pattern exhibits symmetry about the axis $\sin\theta_x = \sin\theta_y$, as shown in Fig. 7(b3). Further increasing φ_x to $\pi/2$ leads to energy redistribution between the central and first-order diffraction peaks along the y-direction, as shown in Fig. 7(b4). Both the energy distribution and symmetry of the diffraction pattern can be efficiently modulated by tuning φ_x and φ_y. These results indicate that when a phase difference exists between the two sublattices along only one direction, the diffracted energy is transferred to its orthogonal direction, while bidirectional (horizontal and vertical) phase differences between the two sublattices enhance the zeroth- and first-order components but leave higher-order components weak.

Furthermore, Figs. 8(a1)–(a4) illustrate the evolution of diffraction intensity as a function of probe detuning

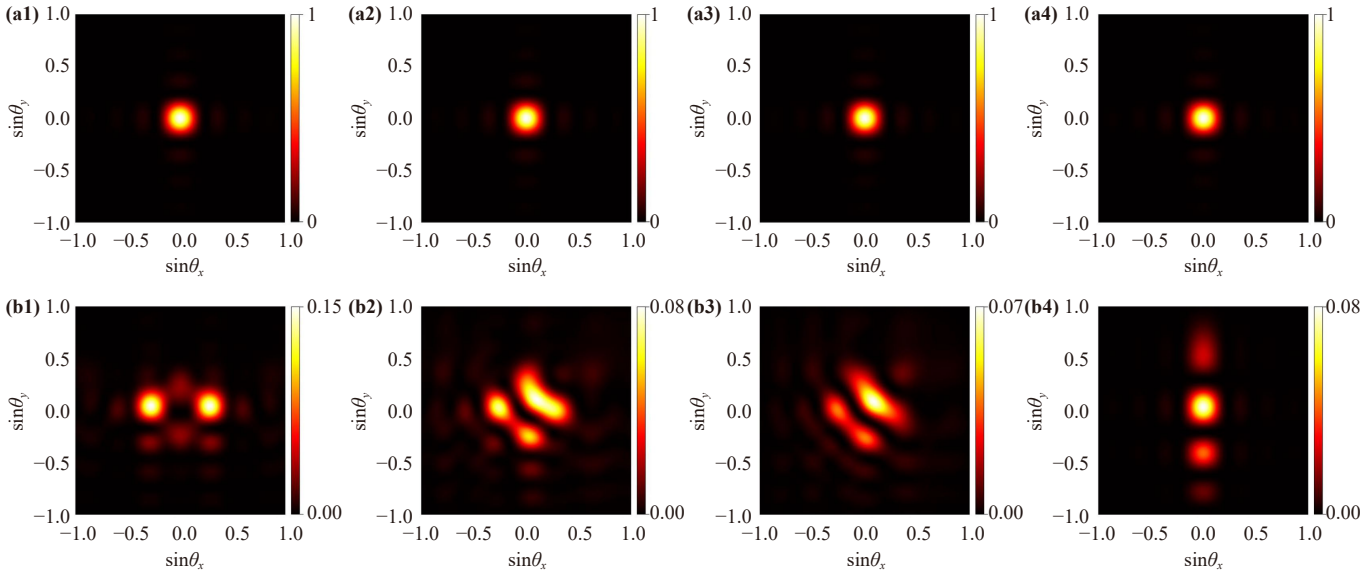

Fig. 7 Far-field diffraction patterns of amplitude- and phase-type photoinduced lattice with different spatial phase difference between the two sublattices, **(a1, b1)** $\varphi_x = 0$, $\varphi_y = \pi/3$, **(a2, b2)** $\varphi_x = \pi/4$, $\varphi_y = \pi/3$, **(a3, b3)** $\varphi_x = \pi/3$, $\varphi_y = \pi/3$, and **(a4, b4)** $\varphi_x = \pi/2$, $\varphi_y = \pi/3$. Other parameters $\Omega_c = 15$ MHz, $\Delta_c = 0$ MHz, $\gamma_{10} = 1$ MHz, $\gamma_{20} = 0.1$ MHz, $L = 12$, and $M = N = 1$.

Δ_p and spatial phase difference φ_y for different diffraction orders with fixed $\varphi_x = 0$. The zeroth-order intensity $I(\theta_x^0, \theta_y^0)$ declines within $|\Delta_p| \approx 15-30$ MHz, accompanied by energy transfer to higher orders and periodic modulation versus spatial phase difference. For the first-order diffraction $I(\theta_x^1, \theta_y^0)$ shown in Fig. 8(a2), the intensity peaks at the designated parameters ($\varphi_y = \pm\pi/2$ and $\Delta_p \approx \pm 25$ MHz) and preserves a symmetric distribution, demonstrating identical responses to positive and negative detuning. In Fig. 8(a3), the intensity of $I(\theta_x^0, \theta_y^1)$ peaks are concentrated near $\Delta_p \approx \pm 30$ MHz and reach their maximum magnitude at $\varphi_y = 0, \pm\pi$. Although local symmetry is broken, the overall pattern still retains approximate centrosymmetry. In contrast, the first-order diffraction in the four quadrants $I(\theta_x^1, \theta_y^1)$ features more localized intensity peaks, as shown in Fig. 8(a4). Its

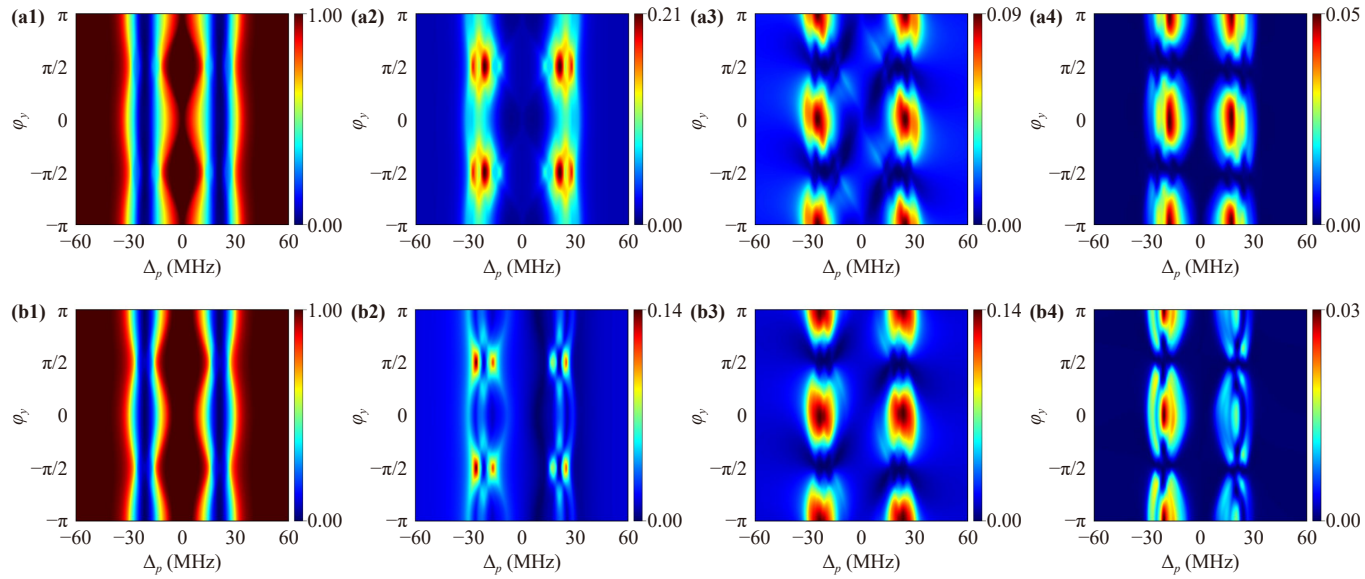

Fig. 8 **(a1–a4)** show the effects of probe detuning Δ_p and spatial phase difference φ_y on the diffraction intensity with fixed $\varphi_x = 0$, (a1) zeroth-order diffraction $I(\theta_x^0, \theta_y^0)$, (a2) first-order diffraction along the x-direction $I(\theta_x^1, \theta_y^0)$, (a3) first-order diffraction along the y-direction $I(\theta_x^0, \theta_y^1)$, and (a4) first-order diffraction in the four quadrants $I(\theta_x^1, \theta_y^1)$. **(b1–b4)** show the effects of Δ_p and φ_y on the diffraction intensity with fixed $\varphi_x = \pi/3$, (b1) $I(\theta_x^0, \theta_y^0)$, (b2) $I(\theta_x^1, \theta_y^0)$, (b3) $I(\theta_x^0, \theta_y^1)$, and (b4) $I(\theta_x^1, \theta_y^1)$. Other parameters $\Omega_c = 15$ MHz, $\gamma_{10} = 1$ MHz, $\gamma_{20} = 0.1$ MHz, $L = 12$, and $M = N = 1$.

overall modulation pattern in the parameter plane $\varphi_y - \Delta_p$ is nearly centrosymmetric, accompanied by slight local intensity imbalance. These results demonstrate that Δ_p modulates the phase response of the medium, thereby enabling effective phase modulation of the probe field, and redistributing diffraction energy across different orders. Moreover, the introduction of the 1D spatial phase difference φ_y breaks the spatial symmetry of the system, which manifests in the frequency domain as an asymmetric diffraction intensity distribution along the relevant axis.

Figures 8(b1)–(b4) depict the diffraction properties under different probe detuning Δ_p and spatial phase difference φ_y with fixed $\varphi_x = \pi/3$. In Fig. 8(b1), the zeroth-order diffraction also exhibits evident intensity attenuation across the detuning range $|\Delta_p| \approx 15 - 30$MHz. Such a range corresponds to the EIT window and reveals efficient energy transfer to higher-order diffraction. As the spatial phase difference varies, the modulation region along the axis evolves periodically and maintains its symmetric distribution relative to $\Delta_p = 0$ MHz. For $I(\theta_x^1, \theta_y^0)$, two intensity bands emerge near $\Delta_p \approx \pm 30$ MHz, with their maxima appearing at corresponding positions $\varphi_y = \pm\pi/2$, as shown in Fig. 8(b2). The diffraction property exhibits an asymmetric distribution with respect to $\Delta_p = 0$, in which the intensity on the negative detuning side is far higher than that on the positive side. This asymmetry physically originates from the spatial phase difference φ_x, which modulates the modulation depth of the coupling field and further induces asymmetric phase modulation. For $I(\theta_x^0, \theta_y^1)$, the intensity peaks at $\Delta_p \approx \pm 25$ MHz and $\varphi_y = 0, \pm\pi$ show a centrosymmetric distribution, as shown in Fig. 8(b3). In comparison, $I(\theta_x^1, \theta_y^1)$ exhibits a highly localized intensity distribution, which is dominant only in the negative detuning region $(\Delta_p < 0)$ and shows pronounced asymmetry with respect to $\Delta_p = 0$, as shown in Fig. 8(b4). This behavior originates from the enhanced real part contribution of the susceptibility of the phase-type lattice under negative detuning. This asymmetry is evidenced by unequal intensity responses under phase inversion $(\varphi \to -\varphi)$, a hallmark of spatial phase difference induced asymmetric diffraction. Such symmetry breaking highlights the excellent controllability of diffraction energy in the 2D phase-type lattice through precise spatial phase difference modulation.

Figures 9(a)–(d) illustrate the intensity distribution of different diffraction orders in phase-type lattices under varied spatial phase difference along the x- and y-directions. Differentiated spatial symmetry properties are identified for each diffraction order, which are inherently determined by the lattice spatial phase modulation. The zeroth-order diffraction $I(\theta_x^0, \theta_y^0)$ presents prominent central symmetry in phase space (φ_x, φ_y), accompanied by periodically distributed intensity along multiple directions, as shown in Fig. 9(a). In contrast, x-directional

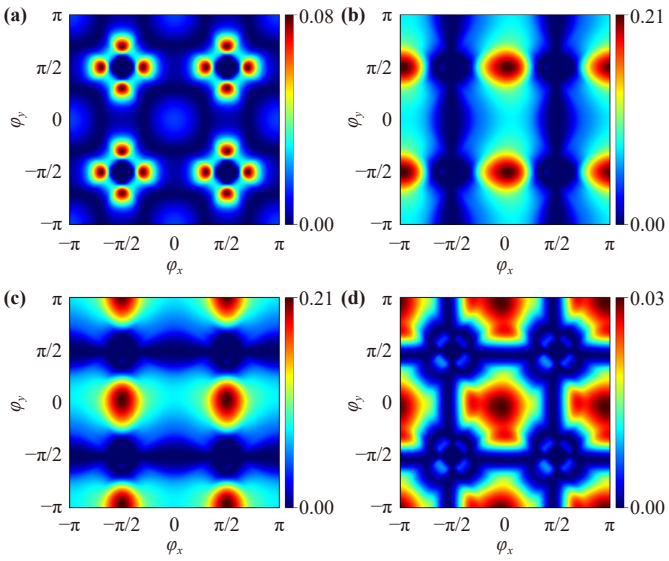

Fig. 9 Diffraction intensity of the phase-type lattice as a function of spatial phase difference along the x- and y-directions, with parameters $\Delta_p = 21.21$ MHz and $\Delta_c = 0$ MHz. **(a)** $I(\theta_x^0, \theta_y^0)$, **(b)** $I(\theta_x^1, \theta_y^0)$, **(c)** $I(\theta_x^0, \theta_y^1)$, and **(d)** $I(\theta_x^1, \theta_y^1)$.

first-order diffraction $I(\theta_x^1, \theta_y^0)$ holds mirror symmetry about $\varphi_y = \pm\pi/2$ axis, as shown in Fig. 9(b), whereas y-directional first-order diffraction $I(\theta_x^0, \theta_y^1)$ is symmetric with respect to $\varphi_x = \pm\pi/2$ axis, as shown in Fig. 9(c). The orthogonal configuration of the above symmetry axes well reveals the spatial anisotropy of the lattice structure. Furthermore, the diffraction symmetry of the first-order diffraction in the four quadrants $I(\theta_x^1, \theta_y^1)$ is broken, while the periodicity along the x- and y-directions is still maintained, as shown in Fig. 9(d). This demonstrates that spatial phase difference modulation exerts a dominant modulation effect on the symmetry and periodicity of diffraction intensity distributions.

4 Conclusion

In summary, we construct a phase-controlled photoinduced lattice in an atomic ensemble by superposing two sublattices via the interference of eight coupling beams. The introduction of spatial phase difference enables precise, dynamic manipulation of the transmission function and far-field diffraction. For the amplitude-type lattice, most optical energy is confined to the zeroth diffraction order; in contrast, for the phase-type lattice, energy is efficiently coupled into higher diffraction orders. The interaction between probe detuning and spatial phase modulates the first-order diffraction intensity periodically, with optimal efficiency achieved within the 15–30 MHz EIT window. Meanwhile, the spatial phase difference governs the directionality and spatial localization of diffraction spots. When the two sublattices are fully in phase, the 2D diffraction pattern retains perfect symmetry. The

introduction of a unidirectional phase difference degenerates the symmetric 2D lattice into a 1D stripe structure. By simultaneously imposing both spatial phase differences, the inherent symmetry is broken, thereby yielding reconfigurable anisotropic 2D modulation patterns. This scheme not only provides a feasible approach to realize dynamically reconfigurable all-optical beam splitters and directional photonic elements, but also serves as a versatile platform for high-precision optical control and integrated quantum photonic applications.

Declarations The authors declare that they have no competing interests and there are no conflicts.

Data availability Data underlying the results presented in this paper are not publicly available at this time but may be obtained from the authors upon reasonable request.

Acknowledgements This work was supported by the XJTU Research Fund for AI Science (No. 2025YXYC004), the National Natural Science Foundation of China (NSFC) (Grant Nos. 62074127, 62404177, U21A2073, 61804122, 11874142, 61627812, 61705176, 11874102, 11474048, 62304175, and 61805068), the Natural Science Foundation of Shaanxi Province (Grant Nos. 2018JQ6002, 2021JQ062, 2021JQ056, and 2021GY223), the Postdoctoral Science Foundation (Grant Nos. 2019M653637, 2019M660256, and 2017M620300), the National Key Research and Development Program of China (Grant No. 2018YFE0125900), the Fundamental Research Funds for the Central Universities (FRFCU) (Grant No. ZYGX2019J102), the National Key Research and Development Program of China (NK R&D PC) (Grant Nos. 2017YFB0402800 and 2017YFB0402802), the Natural Science Basic Research Program of Shaanxi (Program No. 2024JC-YBMS-505), and the XJTU Research Fund for AI Science (No. 2025YXYC004).

References

1. N. Dupuis and K. Sengupta, Superfluid to Mott-insulator transition of cold atoms in optical lattices, *Physica B* 404(3–4), 517 (2009)
2. D. Jaksch, C. Bruder, J. I. Cirac, C. W. Gardiner, and P. Zoller, Cold bosonic atoms in optical lattices, *Phys. Rev. Lett.* 81(15), 3108 (1998)
3. I. Bloch, Ultracold quantum gases in optical lattices, *Nat. Phys.* 1(1), 23 (2005)
4. I. Bloch and M. Greiner, The superfluid-to-Mott insulator transition and the birth of experimental quantum simulation, *Nat. Rev. Phys.* 4(12), 739 (2022)
5. S. Ospelkaus, C. Ospelkaus, O. Wille, M. Succo, P. Ernst, K. Sengstock, and K. Bongs, Localization of bosonic atoms by fermionic impurities in a 3D optical lattice, *Phys. Rev. Lett.* 96(18), 180403 (2006)
6. M. Greiner, O. Mandel, T. Esslinger, T. W. Hänsch, and I. Bloch, Quantum phase transition from a superfluid to a Mott insulator in a gas of ultracold atoms, *Nature* 415(6867), 39 (2002)
7. I. Bloch, J. Dalibard, and W. Zwerger, Many-body physics with ultracold gases, *Rev. Mod. Phys.* 80(3), 885 (2008)
8. M. Aidelsburger, M. Atala, M. Lohse, J. T. Barreiro, B. Paredes, and I. Bloch, Realization of the Hofstadter Hamiltonian with ultracold atoms in optical lattices, *Phys. Rev. Lett.* 111(18), 185301 (2013)
9. N. Goldman, J. C. Budich, and P. Zoller, Topological quantum matter with ultracold gases in optical lattices, *Nat. Phys.* 12(7), 639 (2016)
10. N. R. Cooper, J. Dalibard, and I. B. Spielman, Topological bands for ultracold atoms, *Rev. Mod. Phys.* 91(1), 015005 (2019)
11. O. Morsch and M. Oberthaler, Dynamics of Bose-Einstein condensates in optical lattices, *Rev. Mod. Phys.* 78(1), 179 (2006)
12. M. Aidelsburger, M. Atala, S. Nascimbène, S. Trotzky, Y. A. Chen, and I. Bloch, Experimental realization of strong effective magnetic fields in an optical lattice, *Phys. Rev. Lett.* 107(25), 255301 (2011)
13. M. Atala, M. Aidelsburger, M. Lohse, J. T. Barreiro, B. Paredes, and I. Bloch, Observation of the Meissner effect with ultracold atoms in bosonic ladders, *Nat. Phys.* 10(8), 588 (2014)
14. N. Gemelke, X. Zhang, C. L. Hung, and C. Chin, In situ observation of incompressible Mott-insulating domains in ultracold atomic gases, *Nature* 460(7258), 995 (2009)
15. O. E. Mustecaplioglu and L. You, Super-radiant light scattering from trapped Bose Einstein condensates, *Phys. Rev. A* 62(6), 063615 (2000)
16. J. P. Marangos, Electromagnetically induced transparency, *J. Mod. Opt.* 45(3), 471 (1998)
17. M. Fleischhauer, A. Imamoglu, and J. P. Marangos, Electromagnetically induced transparency: Optics in coherent media, *Rev. Mod. Phys.* 77(2), 633 (2005)
18. L. V. Hau, S. E. Harris, Z. Dutton, and C. H. Behroozi, Light speed reduction to 17 metres per second in an ultracold atomic gas, *Nature* 397(6720), 594 (1999)
19. D. Petrosyan and Y. P. Malakyan, Magneto-optical rotation and cross-phase modulation via coherently driven four-level atoms in a tripod configuration, *Phys. Rev. A* 70(2), 023822 (2004)
20. A. K. Mohapatra, T. R. Jackson, and C. S. Adams, Coherent optical detection of highly excited Rydberg states using electromagnetically induced transparency, *Phys. Rev. Lett.* 98(11), 113003 (2007)
21. M. Bajcsy, A. S. Zibrov, and M. D. Lukin, Stationary pulses of light in an atomic medium, *Nature* 426(6967), 638 (2003)
22. D. F. Phillips, A. Fleischhauer, A. Mair, R. L. Walsworth, and M. D. Lukin, Storage of light in atomic vapor, *Phys. Rev. Lett.* 86(5), 783 (2001)
23. S. M. Hendrickson, C. N. Weiler, R. M. Camacho, P. T. Rakich, A. I. Young, M. J. Shaw, T. B. Pittman, J. D. Franson, and B. C. Jacobs, All-optical switching demonstration using two-photon absorption and the classical Zeno effect, *Phys. Rev. A* 87(2), 023808 (2013)
24. V. Boyer, C. McCormick, E. Arimondo, and P. Lett, Ultraslow propagation of matched pulses by four-wave mixing in an atomic vapor, *Phys. Rev. Lett.* 99(14), 143601 (2007)

25. Q. Glorieux, T. Aladjidi, P. D. Lett, and R. Kaiser, Hot atomic vapors for nonlinear and quantum optics, *New J. Phys.* 25(5), 051201 (2023)
26. Y. W. Cho, K. K. Park, J. C. Lee, and Y. H. Kim, Engineering frequency-time quantum correlation of narrow-band biphotons from cold atoms, *Phys. Rev. Lett.* 113(6), 063602 (2014)
27. L. E. E. de Araujo, Electromagnetically induced phase grating, *Opt. Lett.* 35(7), 977 (2010)
28. Y. Zhang, X. Cheng, X. Yin, J. Bai, P. Zhao, and Z. Ren, Research of far-field diffraction intensity pattern in hot atomic Rb sample, *Opt. Express* 23(5), 5468 (2015)
29. J. Yuan, S. Dong, C. Wu, L. Wang, L. Xiao, and S. Jia, Optically tunable grating in a V + Ξ configuration involving a Rydberg state, *Opt. Express* 28(16), 23820 (2020)
30. T. N. Dey and G. S. Agarwal, Storage and retrieval of light pulses at moderate powers, *Phys. Rev. A* 67(3), 033813 (2003)
31. A. W. Brown and M. Xiao, All-optical switching and routing based on an electromagnetically induced absorption grating, *Opt. Lett.* 30(7), 699 (2005)
32. F. Wen, H. Ye, X. Zhang, W. Wang, S. Li, H. Wang, Y. Zhang, and C. Qiu, Optically induced atomic lattice with tunable near-field and far-field diffraction patterns, *Photon. Res.* 5(6), 676 (2017)
33. J. Gao, C. Hang, and G. Huang, Linear and nonlinear Bragg diffraction by electromagnetically induced gratings with PT symmetry and their active control in a Rydberg atomic gas, *Phys. Rev. A* 105(6), 063511 (2022)
34. S. C. Tian, R. G. Wan, L. J. Wang, S. L. Shu, H. Y. Lu, X. Zhang, C. Z. Tong, J. L. Feng, M. Xiao, and L. J. Wang, Asymmetric light diffraction of two-dimensional electromagnetically induced grating with *PT* symmetry in asymmetric double quantum wells, *Opt. Express* 26(25), 32918 (2018)
35. Z. Chen, X. Liu, and J. Zeng, Electromagnetically induced moiré optical lattices in a coherent atomic gas, *Front. Phys. (Beijing)* 17(4), 42508 (2022)
36. C. Hang, W. Li, and G. Huang, Nonlinear light diffraction by electromagnetically induced gratings with PT symmetry in a Rydberg atomic gas, *Phys. Rev. A* 100(4), 043807 (2019)
37. J. Yuan, C. Wu, L. Wang, G. Chen, and S. Jia, Observation of diffraction pattern in two-dimensional optically induced atomic lattice, *Opt. Lett.* 44(17), 4123 (2019)
38. Y. Gu, F. Wen, M. Zhai, H. Ye, S. Zhang, Z. Wu, D. Zhong, Y. Du, Z. Zhang, W. Wang, Y. Lei, Y. Zhang, and H. Wang, Dynamically tunable optical lattice based on optics and magnetism with nitrogen–vacancy center in diamond, *Opt. Laser Technol.* 184, 112508 (2025)
39. F. Wen, S. Zhang, S. Hui, H. Ma, S. Wang, H. Ye, W. Wang, T. Zhu, Y. Zhang, and H. Wang, Terahertz tunable optically induced lattice in the magnetized monolayer graphene, *Opt. Express* 30(2), 2852 (2022)
40. L. Tarruell, D. Greif, T. Uehlinger, G. Jotzu, and T. Esslinger, Creating, moving and merging Dirac points with a Fermi gas in a tunable honeycomb lattice, *Nature* 483(7389), 302 (2012)
41. F. Niu, H. Zhang, J. Yuan, L. Xiao, S. Jia, and L. Wang, Photonic graphene with reconfigurable geometric structures in coherent atomic ensembles, *Front. Phys. (Beijing)* 18(5), 52304 (2023)
42. F. Wen, X. Zhang, H. Ye, W. Wang, H. Wang, Y. Zhang, Z. Dai, and C. Qiu, Efficient and tunable photoinduced honeycomb lattice in an atomic ensemble, *Laser Photonics Rev.* 12(9), 1800050 (2018)
43. Y. Zhang, Z. Wu, M. R. Belić, H. Zheng, Z. Wang, M. Xiao, and Y. Zhang, Photonic Floquet topological insulator in an atomic ensemble, *Laser Photonics Rev.* 9(3), 331 (2015)
44. M. Zhai, F. Wen, S. Zhang, H. Ye, Z. Wu, J. Li, Z. Sun, B. Wen, W. Wang, F. Lin, Y. Zhang, and H. Wang, Phase sensitivity plasmon resonance enhanced nonlinear diffraction in a hybrid artificial molecule, *Chin. Opt. Lett.* 23(11), 111902 (2025)
45. F. Schäfer, T. Fukuhara, S. Sugawa, Y. Takasu, and Y. Takahashi, Tools for quantum simulation with ultracold atoms in optical lattices, *Nat. Rev. Phys.* 2(8), 411 (2020)
46. M. Zhai, F. Wen, S. Zhang, H. Ye, Z. Wu, D. Zhong, Y. Lei, Y. Gu, W. Wang, M. Zhang, Y. Zhang, and H. Wang, Efficient and tunable photoinduced moiré lattice in an atomic ensemble, *Front. Phys. (Beijing)* 20(3), 34207 (2025)
47. P. Wang, Y. Zheng, X. Chen, C. Huang, Y. V. Kartashov, L. Torner, V. V. Konotop, and F. Ye, Localization and delocalization of light in photonic moiré lattices, *Nature* 577(7788), 42 (2020)
48. X. Liu and J. Zeng, Two-dimensional localized modes in nonlinear systems with linear nonlocality and moiré lattices, *Front. Phys. (Beijing)* 19(4), 42201 (2024)
49. M. Frasca, Theory of dressed states in quantum optics, *Phys. Rev. A* 60(1), 573 (1999)
50. E. K. Twyeffort Irish, Generalized rotating-wave approximation for arbitrarily large coupling, *Phys. Rev. Lett.* 99(17), 173601 (2007)
51. H. Y. Ling, Y. Q. Li, and M. Xiao, Electromagnetically induced grating: Homogeneously broadened medium, *Phys. Rev. A* 57(2), 1338 (1998)
52. B. Wang, D. Yan, Y. Liu, and J. Wu, Two-dimension asymmetric electromagnetically induced grating in Rydberg atoms, *Photonics* 9(10), 674 (2022)
53. J. Yuan, S. Dong, H. Zhang, C. Wu, L. Wang, L. Xiao, and S. Jia, Efficient all-optical modulator based on a periodic dielectric atomic lattice, *Opt. Express* 29(2), 2712 (2021)
54. H. Zhang, J. Yuan, S. Dong, C. Wu, L. Wang, L. Xiao, and S. Jia, All-optical tunable high-order Gaussian beam splitter based on a periodic dielectric atomic structure, *Opt. Express* 29(16), 25439 (2021)